Journal of
Materials Chemistry A

PAPER

View Article Online
View Journal | View Issue

Cite this: *J. Mater. Chem. A*, 2019, 7, 16541

Towards a durable high performance anode material for lithium storage: stabilizing N-doped carbon encapsulated FeS nanosheets with amorphous TiO_2†

Xuefang Xie,‡[a] Yang Hu,‡[a] Guozhao Fang,[a] Xinxin Cao,[a] Bo Yin,[a] Yaping Wang,*[a] Shuquan Liang,[a] Guozhong Cao[b] and Anqiang Pan*[a]

Received 25th March 2019
Accepted 4th June 2019

DOI: 10.1039/c9ta03196k

rsc.li/materials-a

As a promising conversion-type anode material, iron sulfide has been widely studied. However, due to its huge volume expansion during repeated lithiation/delithiation, iron sulfide tends to pulverize and form aggregates upon cycling, which greatly hinders its application in high performance lithium ion batteries as a durable anode material. Herein, a strategy for synthesizing and stabilizing iron sulfide nanosheets with a robust titanium oxide nanofiber interior support is proposed. The hierarchical nanostructured composite anode material was successfully synthesized by the electrospinning technique and subsequent sulfurization. The size of the iron sulfide nanosheets can be easily tuned by adjusting the composition of the reacting agents and/or the sulfurization temperature. Electrochemical results reveal that the composite delivers a reversible capacity of 591 mA h g^{-1} at a current density of 0.1 A g^{-1} after 100 cycles and exhibits excellent long-term cycling stability at 0.5 A g^{-1} and 1 A g^{-1} as well. Furthermore, when being paired with $LiFePO_4$, the as-synthesized composite also delivers promising full-cell performance, showing its potential in serving as a competitive candidate anode material in lithium-ion batteries for power applications. Moreover, this method also opens up an avenue for modifying and improving other conversion-type anode materials.

Introduction

Metal sulfides have attracted extensive attention as alternative LIB anodes due to their high theoretical capacity and good conductivity.[1–10] Among all kinds of metal sulfides, iron sulfide has become more and more popular recently because of the environmental benignity and abundant resources of iron.[2,11–14] However, the same as other sulfides, due to their huge volume fluctuation during charging and discharging, the capacities of iron sulfide anode materials decay rapidly upon cycling, which seriously hinders their practical applications.[11,13,14] To improve the cycling performance of metal sulfides, several effective methods such as combining with elastic and conductive carbonaceous materials,[2,11,12,15–19] constructing spacious hierarchical nanostructures[20–22] and compositing with robust metal oxides[20,23] have been undertaken.

To be specific, Mai *et al.* fabricated an FeS@N–C nanowire composite through a simple amine-assisted solvothermal reaction and subsequent calcination. The as-prepared LIB anode exhibited superior rate capability and long-term cycling stability.[14] Constructing spacious hierarchical nanostructures has also been proved to be effective in improving the cycling performance.[20,24–26] For example, Ma *et al.* synthesized a 3D flowerlike iron sulfide material *via* a facile one-step sulfurization process, finding that its unique structural features can effectively alleviate the volume fluctuations in lithiation/delithiation processes and shorten the diffusion length of lithium ions as well.[25] Moreover, instead of making pure iron sulfide, compositing FeS and metal oxides with a rational design would make good use of the synergistic effect between them and realize better performance. For example, a flower-like Fe_2O_3/FeS composite prepared by Wang *et al.* through a solvothermal method and a subsequent oxidation process showed better cycling stability and rate performance than pure FeS.[20] Among all kinds of metal oxides, TiO_2 especially amorphous TiO_2 or hydrogen treated TiO_2 has been widely used as a sulfur host, protective shell or buffering layer in composite materials due to its rich defects and strong chemical interactions with active materials, which can ensure a prolonged cycling life span.[23,27–32] Furthermore, its small volume change (~4%) upon cycling,

---

[a] *School of Materials Science and Engineering, Central South University, Changsha 410083, Hunan, China. E-mail: pananqiang@csu.edu.cn; yapingwang@csu.edu.cn; Fax: +86-0731-88876692*

[b] *Department of Materials Science and Engineering, University of Washington, Seattle, WA, 98195, USA*

† Electronic supplementary information (ESI) available. See DOI: 10.1039/c9ta03196k

‡ These authors contributed equally to this manuscript.

elastic feature and excellent structural stability also make amorphous TiO_2 perfect for compositing with alloy-type or conversion-type anodes to provide more stability. Yang *et al.* wrapped silicon nanoparticles with amorphous TiO_2 shells to alleviate the violent volume fluctuations of silicon during charging/discharging and achieved improved cycling performance.[28] Amorphous TiO_2 was also used to compose with SnO_2 and served as a buffer layer for realizing better cycling stability.[29] Although TiO_2 has been widely used as a compositing agent in anode materials, usually employed as a protective shell or buffering layer, the use of TiO_2 as a robust support for conversion type anode materials like FeS has not yet been well studied. The electrospinning technique is widely used as an ideal method to construct multi-component hierarchical nanostructured materials due to its convenience and good control of the morphology of products.[26]

Thus, taking into account the advantages of a conductive carbon matrix, spacious hierarchical nanostructure and amorphous TiO_2 buffer layer, we synthesized a novel hierarchical structured FeS@TiO_2@C composite material *via* the electrospinning technique and subsequent sulfurization. Here, the amorphous TiO_2/C nanofiber serves as a robust backbone, which not only helps to stabilize FeS during cycling but also plays an important role in controlling the growth of FeS nanosheets and maintaining the hierarchical nanofibrous morphology. Electrochemical results revealed that the composite anode exhibited a high capacity of 591 mA h g^{-1} after being repeatedly cycled 100 times at a current density of 0.1 A g^{-1} and long-term cycling stability at 0.5 A g^{-1} and 1 A g^{-1}. And a high reversible specific capacity of 465.0 mA h g^{-1} can still be delivered when being cycled at 2 A g^{-1}. More importantly, a $LiFePO_4$//FS@TO full cell also showed good cycling stability and a high reversible capacity.

Experimental

Materials synthesis

Titanium butoxide (TBOT, $C_{16}H_{36}O_4Ti$, CP, 98.0%, Aladdin), acetic acid (AA, CH_3COOH, ≥99.5%, Sinopharm Chemical Reagent Co., Ltd.), iron(III) acetylacetonate ($Fe(acac)_3$, $C_{15}H_{21}FeO_6$, ≥98%, Aladdin), *N*,*N*-dimethylformamide (DMF, C_3H_7NO, ≥99.5%, Sinopharm Chemical Reagent Co., Ltd.), thiourea (H_2NCSNH_2, Sinopharm Chemical Reagent Co., Ltd.), polyvinylpyrrolidone (PVP, M.W. = 1 300 000, Alfa Aesar (China) Chemicals Co., Ltd.) and lithium iron phosphate ($LiFePO_4$, 98.3%, Zhejiang Ruibang technology Co., Ltd.) were all of analytical grade and used without further purification in this work.

First, 0.51 g of PVP was dissolved in 2.49 g of DMF to form a transparent solution under stirring for 3 hours at 40 °C. Then 1 mL of AA was added to the above transparent solution and further stirred for 10 more minutes before 1 mL of TBOT was injected and stirred overnight. Finally, 1 g of $Fe(acac)_3$ was dissolved in the above pale yellow solution and stirred for another 4 hours. The bright red solution was drawn into a 5 mL syringe with a stainless steel nozzle (0.58 mm of inner diameter). Then the solution was ejected and electrospun onto a plate collector covered with aluminum foil that was placed about 15 cm away from the needle, and a voltage of 11 kV was applied between the needle and the plate to initiate the electrospinning. The temperature of the electrospun instrument is set to 35 °C. The resulting orange red nanofibers were collected under a propelling speed of around 0.1 mm min^{-1}.

The FS@TO was prepared by sulfurizing the precursor of FeS@TO nanofibers collected in the electrospinning process mentioned above in a tubular furnace under vacuum. To ensure full sulfurization excess thiourea was used as the sulfur source, and the system was heated to 500 °C with a ramp rate of 2 °C min^{-1}, then maintained for 3 hours before cooling down to room temperature naturally; the as-prepared sample is denoted as FS@TO. For comparison, the TiO_2/C nanofibers and FeS nanosheets were prepared *via* the same procedures without adding an iron source and titanium source, respectively, and the as-synthesized products are denoted as TO and FS. In order to investigate the influence of sulfurizing temperature on the morphology of the final product, the precursor of FS@TO was also sulfurized at 600 °C and 700 °C, and the as-obtained samples are denoted as FS@TO-600 and FS@TO-700.

Characterization

The crystallographic phases of the as-prepared samples were determined by X-ray diffraction (XRD, Rigaku D/Max 2500) using Cu Kα radiation (λ = 1.54178 Å). The microscopic morphology of the material surface was observed using a field emission scanning electron microscope (FESEM, FEI Nova NanoSEM 230). A Titan G2 60-300 TEM was used to further obtain TEM and HRTEM images and energy dispersive spectrometer mapping in order to obtain more structural details. The data of the element composition and content, chemical state, molecular structure and chemical bonds of the compound are provided by X-ray photoelectron spectroscopy (XPS). Elemental carbon and sulfur contents in the sample were determined using a C–S analyzer (LECO CS600, America). TG and DSC tests were carried out on a STA449C (NETZSCH, Germany) from room temperature to 700 °C with a heating ramp of 10 °C min^{-1}. ICP-OES (Optima5300DV) was employed to determine the content of Fe and Ti elements. Specific surface areas were calculated using the multi-point Brunauer–Emmett–Teller (BET) method. The pore size distribution was calculated from the adsorption branch using the nonlocal density functional theory (NLDFT) model.

Electrochemical measurements

Stainless-steel coin cells (CR2016) used for electrochemical measurements were assembled in a glovebox filled with high-purity argon gas. The working electrodes were obtained by coating a homogeneous aqueous slurry containing 80% active materials, 10% Super P and 10% sodium carboxymethyl cellulose (CMC) onto copper foil before being dried in a vacuum oven at 100 °C overnight. Lithium foil was used as the counter/reference electrode, and 1 M $LiPF_6$ in a mixture of dimethyl carbonate (DMC), ethylene carbonate (EC) and ethyl methyl carbonate (EMC) (1 : 1 : 1 by volume) was chosen as the electrolyte. Cyclic voltammetry (CV) curves were recorded using an electrochemical workstation (CHI660C, Shanghai), and electrochemical impedance spectroscopic analysis (EIS) from 100 kHz to 10 mHz was conducted on an electrochemical workstation (MULTI AUTOLAB M204, Metrohm). The galvanostatic charge/discharge performances were studied in the potential range of 0.01–3 V (*vs.* Li^+/Li) using a multichannel battery testing system (Land CT 2001A).

For the full battery assembly, commercial $LiFePO_4$ (98.3%, Zhejiang Ruibang Technology Co., Ltd.) was used as the cathode material and mixed with acetylene black and polyvinylidene fluoride (PVDF) with a weight ratio of 7 : 2 : 1 before dispersing in NMP to form a uniform aqueous slurry, which was then applied onto aluminum foil and dried in a vacuum oven at 100 °C. To ensure the full utilization of the FS@TO composite anode, the $LiFePO_4$ electrode was punched into larger discs (Φ16) than the anode ones (Φ12), and the capacity N/P ratio was about 1 : 1.2.

Results and discussion

In this work, we proposed the *in situ* formation of FS@TO, FS and TO composites embedded in nitrogen-doped carbon nanofibers *via* the electrospinning technique and subsequent vacuum sulfurization; the synthesis procedures of FS@TO are schematically shown in Fig. 1. During the stirring and electrospinning procedures, the ferrous source ($Fe(acac)_3$) and titanium source (TBOT) were able to homogeneously disperse in a continuous and uniform carbonaceous matrix derived from PVP, which ensured the alleviation of violent volume change, the inhibition of agglomeration and better electronic conductivity. Then, after being vacuum sulfurized in a tubular furnace, the nanofiber-shaped precursors were successfully converted into the final products with good morphology retention.

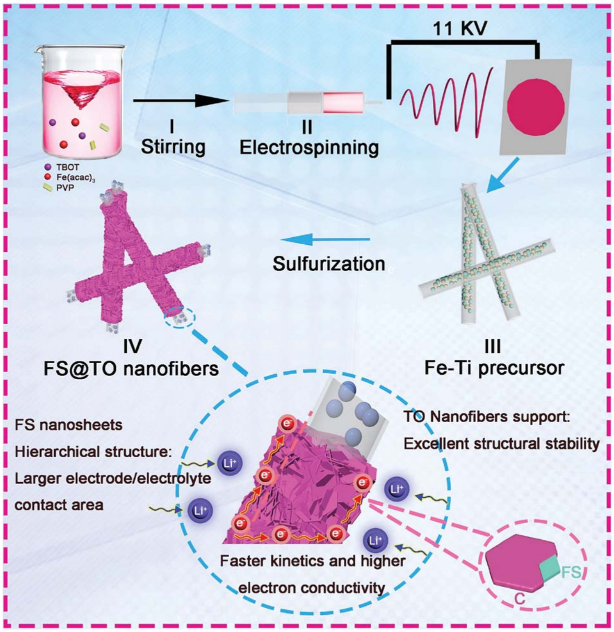

Fig. 1 Schematic illustration of synthesis of FS@TO composite nanofibers.

X-ray diffraction (XRD) patterns of the FS@TO, FS and TO samples obtained at 500 °C are shown in Fig. S1.† All of the visible diffraction peaks of the FS sample can be indexed to the hexagonal FeS phase (JCPDS card no. 89-6927). The sharp peaks corresponding to (110), (112), (114), and (300) planes indicate the good crystallinity of FeS. And the XRD pattern of the TO sample reveals its amorphous feature and poor crystallinity, which is reasonable, as 500 °C is not sufficient for the formation of titanium oxides with good crystallinity. According to the HRTEM image (Fig. S4c†) and Raman spectrum (Fig. S7†), which will be discussed later, the formation of amorphous TiO_2 can be confirmed. As for the FS@TO sample, its XRD pattern is like a superimposition of patterns of both FS and TO samples, indicating the good crystallinity of synthesized FeS and the amorphous feature of the TiO_2 support.

In order to identify the morphology of the as-synthesized products, scanning electron microscopy (SEM) was employed. As shown in Fig. S2,† before sulfurization, precursors of FS@TO (Fig. S2a†), FS (Fig. S2b†) and TO (Fig. S2c†) are all interconnected nanofibers with spacious gaps and a smooth surface. After being sulfurized at 500 °C for 3 h, the FS sample, however, underwent a dramatic morphology change and turned into densely packed thick sheets with a polygon-like shape, whose lateral sizes are roughly around 1 μm (Fig. S3a and b†). This dramatic morphology change could be resulting from the crystallization and growth of FeS grains. Before sulfurization, the iron source was just ions that were glued and wrapped up by PVP, showing a typical fibrous morphology after the electrospinning process. Then, when being heated up with thiourea, the iron source began to react with the sulfurous atmosphere that was given off by the thermolysis of thiourea and formed FeS nanocrystals, which then grew up into polygon-like nanosheets due to its hexagonal crystal structure and became so large that the carbonaceous wrapper derived from PVP was also bulked up by these thick FeS sheets and resulted in a sheet shape rather than a fibrous one. Interestingly, under the same conditions, the morphology of TO did not change significantly before and after sulfurization, as shown in Fig. S2c, S4a and b (ESI†). This phenomenon should be ascribed to the amorphous feature of the as-synthesized TiO_2, as 500 °C was not high enough for the formation of crystalline TiO_2. As a result, the nanofibrous micromorphology was successfully retained. Similarly, as shown in Fig. 2a and b, the as-prepared FS@TO sample also well retained the nanofibrous morphology of its precursor. It can be seen that there are uniformly distributed nanoscale thin sheets on the surface of the fibers. It is worth mentioning that, compared to the nanosheets in the FS sample, the FeS nanosheets in FS@TO are much smaller and thinner, corresponding well to the XRD results shown in Fig. S1:† the sharper and narrower peaks observed in the pattern of the FS sample also indicate that the FeS in the FS sample has better crystallinity and larger sizes. These results suggest that the amorphous titanium oxide in sample FS@TO suppressed the growth of FeS crystals, and thus they successfully retained the nanofibrous morphology instead of growing into thick and large sheets like

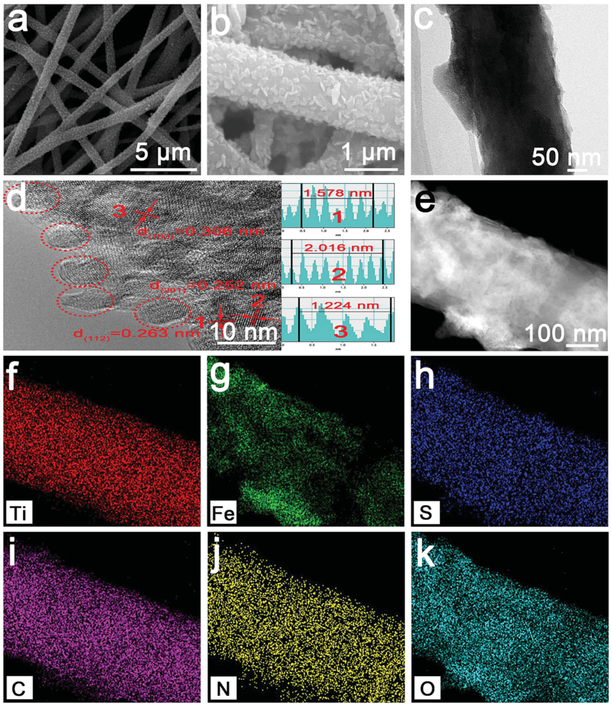

Fig. 2 SEM images (a and b), TEM images (c), the high-resolution TEM image (d), and elemental mapping images (e–k) of FS@TO composite nanofibers.

the FS sample (Fig. S3a and b†). With regard to the unique morphology of the FS@TO sample, here is our proposal for its morphology evolution mechanism. Before sulfurization, as the reagents were uniformly dispersed in the viscous fluid, the iron species and titanium species should be still uniformly distributed in the nanofibers after electrospinning. Then, during the sulfurization process, thiourea decomposed and gave off a sulfurous atmosphere when being heated up, and iron species and titanium species gained higher mobility due to high temperature. For the titanium species, as 500 °C was not high enough for sulfurizing titanium, the titanium species could move randomly, while the iron species kept reacting with the sulfurous atmosphere and forming FeS nanosheets on the surface, and thus the iron species near the surface was consumed by the reaction. Driven by the concentration gradient, the iron species kept moving outward and underwent reaction, and as a result, the obtained FeS nanosheets were all located on the surface of the nanofibers rather than uniformly distributed within the nanofibers. As for the amorphous titanium oxide, although it did not participate in the sulfurization, it interacted with the iron species and slowed down their outward motion rate, and as a result, the FeS crystal sizes in sample FS@TO are much smaller and thinner than those in sample FS whose iron species moved outward more freely. For sample FS@TO, retaining the spacious nanofibrous morphology can not only shorten the ion diffusion distance and provide a continuous electronically conductive matrix, but also accommodate the drastic volume fluctuation of FeS during the repeated (de)lithiation. And the small crystal size of FeS nanosheets also makes it easier to accommodate the nanosheets, and the defects of amorphous TiO_2 backbones keep the FeS nanosheets anchored and avoid agglomeration. According to the BET results shown in Fig. S5 and Table S1,† the TO sample has the largest specific surface area (75.4 $m^2\ g^{-1}$, based on S_{Langmuir}), which should be attributed to its amorphous feature. The FS@TO sample, consisting of amorphous TiO_2 backbones and small FeS nanosheets, possesses a specific surface area of 49.3 $m^2\ g^{-1}$, while the smallest specific surface area of 7.9 $m^2\ g^{-1}$ is observed for FeS. The corresponding pore size distribution curves of FS@TO and FS indicate that the addition of TiO_2 increases the number of micropores (pore sizes below 2 nm). The influence of temperature in the sulfurization process on the morphology of the as-prepared composites was also investigated. Keeping other conditions unchanged, the FS@TO composite nanofibers were also sulfurized with thiourea under vacuum at 600 °C and 700 °C, and the obtained products are denoted as FS@TO-600 and FS@TO-700, respectively. As shown in Fig. S6a,† an uneven distribution and obvious agglomeration of nanosheets can be observed on the surface of the fibers in sample FS@TO-600. When the sulfurization temperature was further increased to 700 °C, iron sulfide sheets grew even larger and stacked with each other resulting in sparsely distributed thick polygon plates, most of which became so large that they can no longer stay connected to the titanium oxide fibers (Fig. S6b†). This can be ascribed to the higher mobility of iron species with elevated temperatures. As discussed above, amorphous titanium oxide played an important role in slowing down the outward motion of Fe species in the sulfurization process, resulting in a well retained nanofibrous morphology at 500 °C. But at higher sulfurizing temperatures (600 °C and 700 °C), this slowing down effect became less effective due to the higher mobility of iron species. And as a result, the FeS crystals grew larger and started to agglomerate.

Fig. 2c shows the TEM image of FS@TO composite nanofibers; it can be seen that the nanosheet attached to the nanofiber is very thin. Fig. 2d shows the HRTEM image of FS@TO, which reveals that the thin nanosheet is composed of many small grains (marked by red dashed line circles), and those planes marked as 1, 2 and 3 can be assigned to (112), (201) and (103) of the FeS phase, respectively, confirming that the thin nanosheets attached on the surface of the nanofibers are crystalline FeS. Fig. 2e shows the high-angle annular dark-field (HAADF) image of a single FeS@TO nanofiber. And Fig. 2f–k are corresponding elemental mapping images of elements Ti, Fe, S, C, N and O, respectively. As seen in Fig. 2g, the distribution of the Fe element matches well with the nanosheet morphology on the surface of the nanofiber in Fig. 2e, which once again confirmed that these nanosheets are FeS. As for the S element distribution (Fig. 2h), instead of overlapping with the Fe one, the S element is uniformly distributed throughout the whole nanofiber. This could be resulting from the reaction between the excess sulfurous atmosphere with the carbonaceous matrix derived from PVP during the sulfurization. As shown in Fig. 2f and i–k, elements Ti, C, N and O are all uniformly distributed throughout the whole nanofiber, indicating the formation of titanium oxide backbones and a

N-doped carbon conducting matrix. The distribution of element O in Fig. 2k seems also overlapping with the distribution of element Fe (Fig. 2g), and this could be attributed to two possible reasons. The overlapping O may come from the oxygen-containing groups that are connected to the carbon matrix that wraps the FeS nanosheets, as the reagent PVP we used in the electrospinning process contains C═O bonds. But also, it may come from some trace Fe_xO_y that formed in the preparation of the test sample or during transportation to the lab for TEM characterization. The observed sample FS was also investigated by TEM and the results are shown in Fig. S3c and d.† It can be seen that the FS sample is composed of unevenly distributed nanoparticles or sheets that are surrounded by amorphous carbon. Fig. S3e† shows the HRTEM of FS, in which clear lattices can be seen and the two lattices marked as 1 and 2 can be assigned to the (004) and (110) planes of hexagonal FeS, respectively. Fig. S3f–k† display the elemental mapping images of the FS sample, which confirmed the even distribution of elements Fe and S, indicating that the whole sheet is FeS. The distribution of element C, however, looks sparser than Fe and S, and the element N is distributed even sparser, suggesting that the uncontrolled growth of FeS crystals broke through the confinement of the outside carbon matrix, which would result in poor cycling performance. The existence of element O could be due to the C═O bonds in the carbonaceous matrix derived from PVP ($(C_6H_9NO)_n$). As for the TO sample, the elemental mapping images (Fig. S4e and g–i†) show the uniform distribution of elements Ti, C, N and O in the nanofibers, confirming the formation of titanium oxides and the N-doped carbonaceous wrap. The existence of element S (Fig. S4f†) can be ascribed to the small amount of C–S bonds formed during the vacuum sulfurization process.

The Raman spectra of samples FS@TO, FS and TO are presented in Fig. S6.† The two strong humps at 1335 cm^{-1} (D band) and 1580 cm^{-1} (G band) can be attributed to the defects of the disordered carbon matrix and in-plane vibration (E_{2g} mode) of sp^2-hybridized graphitic carbon atoms, respectively.[33] In addition, the peak intensity ratio of I_D/I_G is regarded as a useful index to evaluate the degree of crystallinity of the carbonaceous matrix. That is, the bigger the I_D/I_G ratio is, the more defects there are in the characterized sample;[34] it can be seen from these Raman spectra that the carbon matrices in all three samples are mostly amorphous. In the low frequency region, sample TO has 3 small peaks located at 151, 428 and 626 cm^{-1}, which can be assigned to the E_g, B_{1g} and E_g modes of the anatase phase TiO_2, respectively.[35,36] It is worth mentioning that for well crystalline anatase TiO_2, the peak corresponding to the E_g vibration mode should originally be located at 144 cm^{-1}. However, in our sample, this peak is shifted to 151 cm^{-1}, and the shifting phenomenon was also observed by W. F. Zhang *et al.*, who found that this shifting was related to the crystal size of anatase TiO_2.[36] In their work, when the crystallite size of anatase TiO_2 changed from 27.9 to 6.8 nm, the Raman peak shifted from 144 to 151 cm^{-1}. Accordingly, the shifting phenomenon observed in the sample TO confirms the formation of amorphous TiO_2 with tiny crystal size. And the two peaks at 220 and 285 cm^{-1} seen in sample FS confirm the formation of FeS.[37–39] As for the FS@TO sample, the peaks related to anatase TiO_2 and FeS can all be observed in the Raman spectrum, which is strong evidence of the co-existence of both FeS and TiO_2 in the as-synthesized FS@TO composite. And the E_g mode peak of TiO_2 further shifted to 153 cm^{-1}, revealing the amorphous feature of TiO_2 in the composite. Fig. S8a† shows the thermogravimetric analysis (TGA) and differential scanning calorimetry (DSC) results of FS@TO, which contain four stages of weight changes. The first weight loss at about 50–150 °C can be ascribed to the evaporation of physically adsorbed water in the FS@TO composite. And the following weight increase at approximately 200–310 °C corresponds to the oxidation of the FeS into $FeSO_4$.[21] The second steep weight loss takes place at approximately 320–500 °C accompanied by a strong exothermal peak around 423.5 °C, which can be ascribed to the burning off of the carbon matrix and the full oxidation of remaining FeS into Fe_2O_3.[21] The last weight loss stage between 500 and 620 °C is attributed to the further oxidation and decomposition of $FeSO_4$ to produce Fe_2O_3.[21,40] As shown in Fig. S7b,† the TG curve of the FS sample is almost the same as that of FS@TO, showing 3 weight loss and 1 slight weight increase stages that can be explained by the same reactions mentioned above. Its DSC curve, however, shows an additional exothermal peak centered at 350.6 °C. Actually, with a closer look at Fig. S8a,† it is not hard to find that there is also a shoulder peak at around 350 °C. This difference should be ascribed to the smaller size and richer defects of FeS in sample FS@TO, which make the oxidation of FeS less distinguishable from the combustion of carbon. The TG curve of the TO sample is simpler (Fig. S8c†), with only three weight loss stages that can be ascribed to the evaporation of physically adsorbed water and combustion of the carbon shell, respectively. The higher weight loss percentage in the second weight loss stage of FS and TO than that of FS@TO can be ascribed to the higher carbon contents in FS and TO than in FS@TO. As the 29.5% weight loss in FS@TO includes not only the loss of carbon that gets burned off, but also the loss corresponding to the conversion from FeS to Fe_2O_3, C–S analysis was also conducted to obtain more accurate carbon mass content in sample FS@TO. As seen in Table S1,† FS@TO contains 23.52% carbon and 19.44% element S. EDS was also employed and the results are shown in Fig. S9 and Table S3.† The average mass percentage of C and N is about 33.3%, which is consistent with the result obtained from TGA. Table S4† shows the test results of ICP-OES; the atomic ratio between Ti and Fe is 1.082 : 1. So the mass ratio between amorphous TiO_2 and FeS is calculated to be 0.983 : 1.

X-ray photoelectron spectroscopy (XPS) measurements were conducted to ascertain the surface chemical compositions and valence states of the FS@TO. The XPS survey spectrum of the FS@TO nanofibers is shown in Fig. 3a. The high resolution survey spectra regarding elements iron, titanium, sulfur, carbon and nitrogen are shown in Fig. 3b–f, respectively. In the Fe 2p spectrum of the FS@TO nanofibers (Fig. 3b), the two sharp peaks at 711.1 eV and 725.0 eV correspond to Fe^{3+}, while the peaks located at 707.2 eV, 713.0 eV and 719.0 eV indicate the presence of Fe^{2+} in the composite.[41,42] The existence of Fe^{3+} should be ascribed to the formation of Fe_3O_4,[43] which is

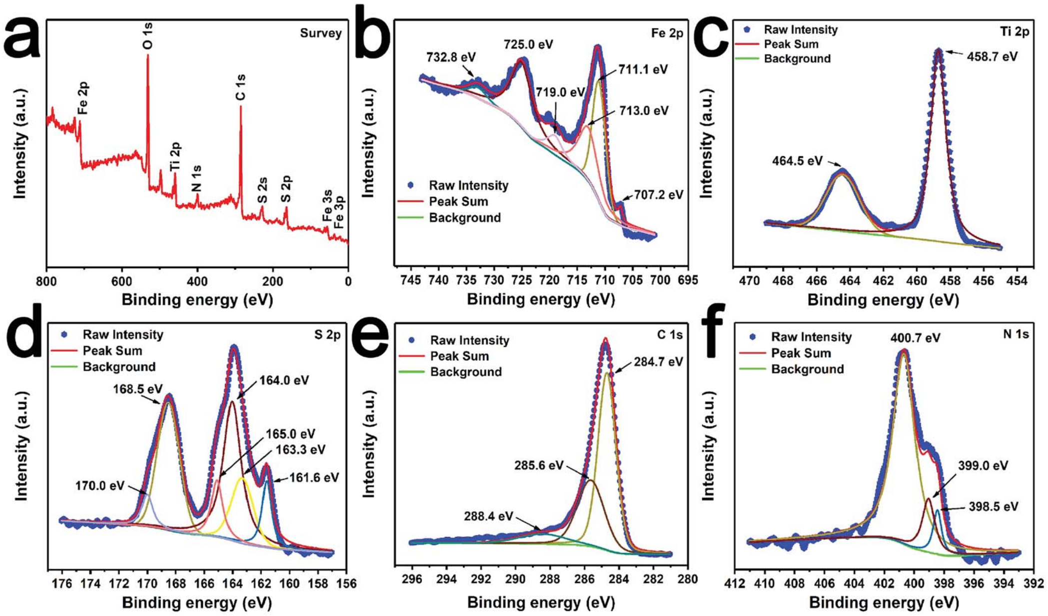

Fig. 3 Typical XPS survey spectra (a) and the high resolution spectra of corresponding elements: Fe 2p (b), Ti 2p (c), S 2p (d), C 1s (e), N 1s (f) of the FS@TO.

reasonable, as FeS is highly reactive toward oxygen and so some FeS could be converted to Fe_3O_4 during the transportation for the XPS test, and a similar phenomenon was also seen in other work.[21] The high resolution Ti 2p spectrum shown in Fig. 3c presents two peaks at 458.7 eV and 464.5 eV, which correspond to Ti $2p_{3/2}$ and Ti $2p_{1/2}$, respectively, indicating the presence of Ti^{4+}.[44–47] Fig. 3d shows the S 2p XPS spectrum, which is a little bit complicated. The peaks at 161.6 eV, 163.3 eV, 165.0 eV, and 164.0 eV confirm the existence of S^{2-}, while the other one at 168.5 eV is attributed to $SO_3{}^{2-}$, which could be resulting from the oxidation of FeS during the transportation for the XPS test.[40,48–51] In the C 1s core-level XPS spectrum shown in Fig. 3e, the peaks at 284.7 eV, 285.6 eV and 288.4 eV can be attributed to C–C, C–N or C–S, and C=O groups, respectively,[52–54] suggesting the presence of N-containing and/or S-containing and O-containing functional groups on the surface of the carbonaceous matrix. The formation of the nitrogen doped carbon matrix can be further confirmed from the N 1s core-level spectrum (Fig. 3f); the peaks at 398.5 eV, 399.0 eV, and 400.7 eV are ascribed to pyridinic nitrogen, pyrrolic nitrogen and graphitic nitrogen, respectively, which provide more evidence for the successful doping of nitrogen in carbon.[55–57] The doped nitrogen atoms can improve the electronic conductivity of carbon, especially pyrrolic N and pyridinic N, which could create numerous extrinsic defects and active sites in the carbon matrix, leading to fast reaction kinetics and good rate capability.[52,55,57–59]

In order to evaluate and compare their electrochemical performances, the as-synthesized products were assembled into two-electrode coin-type half cells by pairing with lithium metal discs as both the counter electrode and reference electrode. Fig. S9a† shows the first five consecutive cyclic voltammetry curves of FS within the voltage window of 0.01–3 V (*vs.* Li^+/Li) at a scan rate of 0.1 mV s^{-1}. In the first cathodic scan, the broad hump from around 1.4 V to 1.099 V can be ascribed to the reaction of Li with FeS forming Li_2FeS_2 ($2FeS + 2Li + 2e = Li_2FeS_2 + Fe$).[42,60] The small hump centered at 0.757 V corresponds to the conversion reaction between FeS and Li ($FeS + 2Li + 2e = Li_2S + Fe$).[42,60] The hump at around 0.353 V, which is absent in the following cycles, can be attributed to the formation of a SEI layer.[42] After the first cycle, the CV curves from the 2nd to 5th cycle are almost overlapped, indicating good reversibility of the FS sample. And the redox pair at 1.432 and 1.882 V can be attributed to the reversible lithiation and delithiation process between $Li_{2-x}FeS_2$ and Li_2FeS_2 (ref. 42) (Fig. S10b).† The CV curves of the TO sample are shown in Fig. S11a,† and no obvious peaks can be observed, indicating the amorphous feature of the TO sample. As for the CV curves of the FS@TO sample (Fig. 4a), the redox pair at 1.429 and 1.879 V is much weaker than the one seen in the CV curves of sample FS; this should be ascribed to the poorer crystallinity and smaller amount (the CV curves were normalized with the active mass of the electrode, and sample FS@TO has less FeS than FS, as the former one also contains a large portion of TiO_2 inside) of FeS in the sample FS@TO. Moreover, the richer defects in the smaller and thinner FeS nanosheets of the FS@TO sample make the lithiation/delithiation process in FS@TO become more consecutive and surface-controlled, thus leading to a less intensive redox pair, which can also be inferred from its increased portion of capacitive contribution (Fig. 5d and S11d†). And it is worth mentioning that although this redox pair is much more obvious in the CV curves of the FeS sample, the capacity delivered is not very impressive (Fig. S10b†). Apart from those peaks also seen in the FS sample, there is a pair of redox peaks located at 1.629 V and 2.334 V, which is not usually seen in other FeS anode studies. This redox pair could be related to

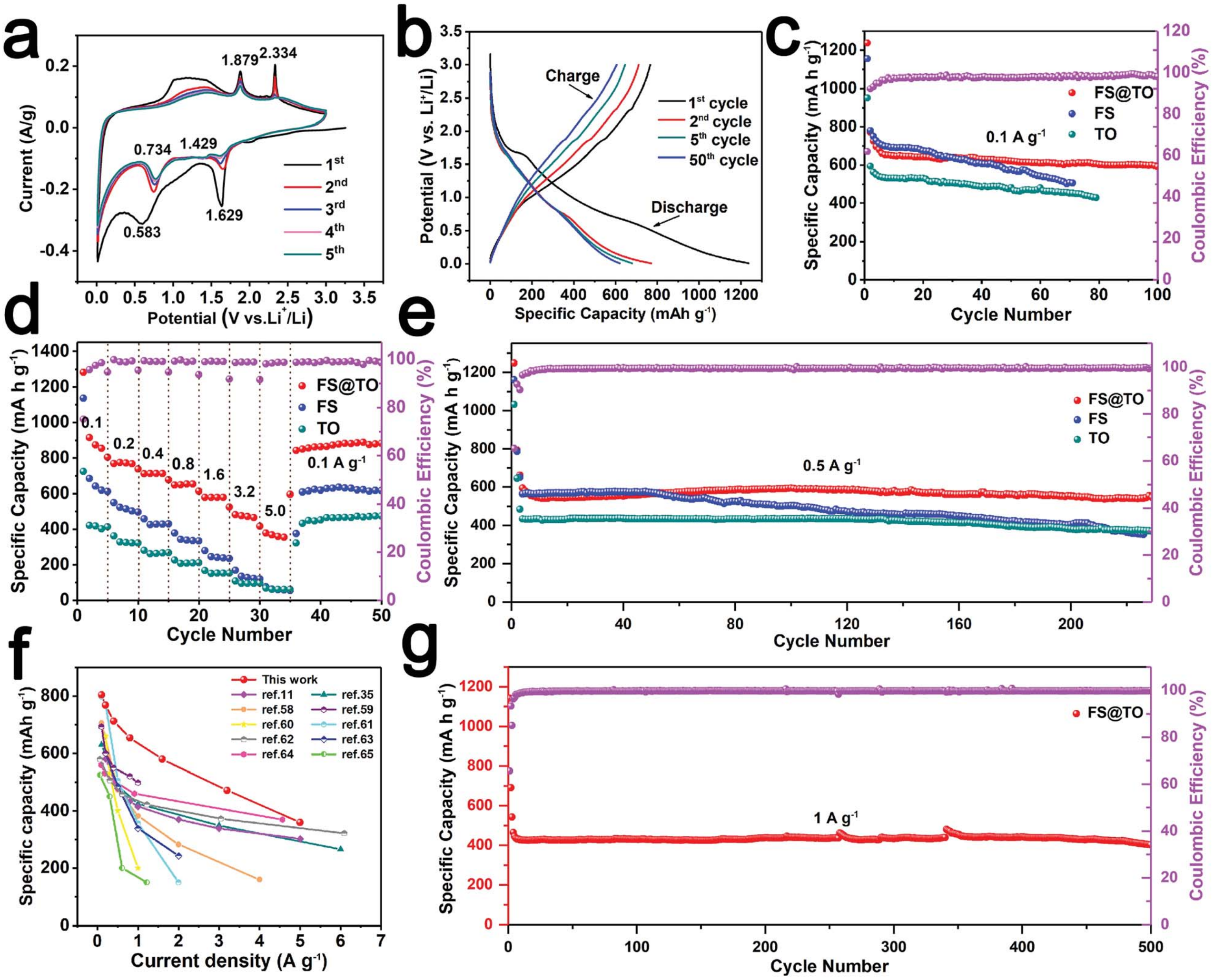

Fig. 4 Electrochemical performance for LIBs: CV curves (a) at 0.1 mV s^{-1} within the voltage range of 0.01–3.0 V *versus* Li$^+$/Li; the initial, second, fifth and fiftieth discharge/charge profiles (b) of the FS@TO at 0.1 A g^{-1}; cycling performances (c) of the FS@TO, FS and TO at 0.1 A g^{-1}; rate performances (d) of the FS@TO, FS and TO at different current densities; long-term cycling performances (e) of the FS@TO, FS and TO at 0.5 A g^{-1}; (f) comparison plot of rate performance between this work and previously published FeS related studies and long-term cycling performances (g) of the FS@TO at 1.0 A g^{-1}.

the conversion between lithium polysulfides and lithium sulfide that usually takes place in Li–S batteries due to the small amount of sulfur absorbed by the pores and defects of the carbonaceous matrix. Da-Wei Wang *et al.*[61] synthesized a microporous–mesoporous carbon filled with sulfur and tested it as a cathode material in a Li–S battery with the electrolyte of 1 M LiPF$_6$ in EC/DMC/EMC (1 : 1 : 1, vol), similar to the electrolyte used in this work. The redox peaks reported in their work are centered at 1.62 V and 2.22 V, which match well with those seen in the CV curves of the FS@TO sample. As seen in Fig. 4a, this pair of redox peaks fades away rapidly in the following cycles which could be due to the irreversible reaction between lithium polysulfides and carbonate solvents in the electrolyte.[62–64] Fig. 4c (the coulombic efficiencies shown in Fig. 4c–e and g all correspond to the FS@TO sample) shows the comparison of the cycling stability of FS@TO, FS and TO at a current density of 0.1 A g^{-1}; it can be seen that the specific discharge capacities in the 2nd cycle of FS@TO (770.8 mA h g^{-1}) and FS (780.6 mA h g^{-1}) are comparable. The capacities of FS in the first 25 cycles are even slightly higher than those of FS@TO, which should be attributed to the larger FeS portion contained in the FS sample. However, due to its larger crystal size, better crystallinity and lack of suitable support backbones, FS undergoes much more severe capacity fading throughout the test compared to FS@TO. As a result, the capacity of FS decreases to 507.7 mA h g^{-1} from 780.6 mA h g^{-1} in 70 cycles with a poor capacity retention of 65.0%. FS@TO, on the other hand, retains 77.4% of the capacity delivered in the 2nd cycle after being cycled for 100 times. Moreover, if the first few cycles are not considered, which are not quite stable due to the formation of an SEI layer, the capacity retention of FS@TO from the 8th to 100th cycle is as high as 91.6% compared to the 72.5% (from the 8th to 71st cycle) for the FS sample. The TO sample shows similar cycling behavior to FS@TO and good capacity

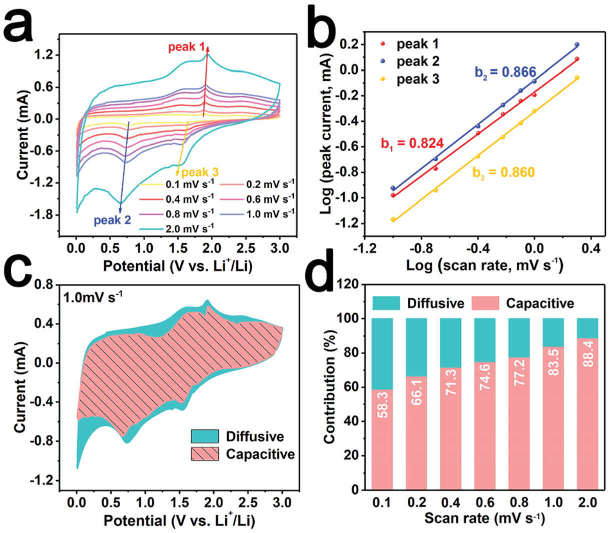

Fig. 5 CV curves (a) at different scan rates from 0.1 to 2.0 mV s^{-1} of the FS@TO, corresponding log(*I*) *versus* log(*v*) plots (b) at specific peak currents, diffusive contribution (mint green) and capacitive contribution (pink) (c) at 1.0 mV s^{-1}, and the percentage of pseudocapacitive contribution (d) at different scan rates.

retention, despite its relatively low specific capacity, which once again proves the good stability of the amorphous TiO_2 backbone and its important role in ensuring the outstanding cycling stability of FS@TO. Similar cycling performances were also obtained at a larger current density of 0.5 A g^{-1} (the first two cycles were cycled at 0.1 A g^{-1} for better activation), and the results are shown in Fig. 4e. Fig. 4b shows the charge/discharge profiles of the 1st, 2nd, 5th and 50th cycles of FS@TO from the galvanostatic cycling test (0.1 A g^{-1}). Consistent with the CV test results, in the initial discharge profile, there is a small plateau at around 1.63 V, which becomes much smaller and can barely be seen in the 2nd cycle. The initial discharge and charge capacities are 1237.8 and 766.4 mA h g^{-1}, respectively, and the huge irreversible capacity loss should be mostly caused by the formation of the SEI layer. The rate performances of these three samples are compared in Fig. 4d. When being cycled at 0.1, 0.2, 0.4, 0.8, 1.6, 3.2, and 5 A g^{-1}, the FS@TO electrode delivers high discharge specific capacities of 914.7 (2nd cycle), 767.8, 712.2, 654.1, 579.4, 471.2 and 359.8 mA h g^{-1}, respectively. After being cycled at 5 A g^{-1}, a high specific capacity of 842.5 mA h g^{-1} can be restored when the current density is switched back to 0.1 A g^{-1}, which then gradually increases to around 880 mA h g^{-1} as the cell becomes stable. Considering that the N-doped carbon matrix also has the ability to store Li^+, the sample N–C was synthesized *via* the same processes (electrospinning and vacuum sulfurization) as that for FS@TO without adding iron(III) acetylacetonate or titanium butoxide. The electrochemical performance of the derived N–C electrode was investigated in a half battery. As shown in Fig. S12,† the electrode N–C delivers a specific discharge capacity of around 300 mA h g^{-1}. As the mass percentage of N-doped carbon in the FS@TO composite is about 33.3%, it can be estimated that N-doped carbon contributes around 100 mA h g^{-1} to the total capacity of 880 mA h g^{-1} in the FS@TO composite. As for the TO sample, although its specific capacity is relatively low, its rate capability is impressive, indicating the good stability of the TiO_2/C nanofiber backbones. With regard to the FS sample, however, without the support of TiO_2/C nanofiber backbones, it suffers more obvious capacity fading as the current density goes higher. At 5 A g^{-1}, its specific capacity (55.6 mA h g^{-1}) even has been surpassed by that of the TO sample (61.1 mA h g^{-1}), not to mention that of the FS@TO sample. To further manifest the good structural stability and electrochemical performance of the as-prepared FS@TO anode, previously published FeS and FeS composite anode materials[15,42,65–71] are also taken into consideration for comparison and the results are shown in Fig. 4f and Table S5.† As shown in Fig. 4f, the FS@TO anode presented in this work delivers higher specific capacities at various current densities than those previously published FeS anodes for LIBs, which strongly supports that the as-synthesized FS@TO composite is a promising and high-performance anode material for lithium storage. Table S5† also shows the comparison of the cycling stabilities of these published FeS anodes with that of the FS@TO electrode in our work and it can be clearly seen that the FS@TO anode shows competitive long-term cycling performance. The long-term cycling performance of the FS@TO electrode at high current density was also evaluated, and the result is shown in Fig. 4g. The same as the test at 0.5 A g^{-1}, before being cycled at 1 A g^{-1}, the cell was cycled at 0.1 A g^{-1} for the first two cycles. Putting aside the first two cycles that were cycled at 0.1 A g^{-1} and the transition cycle (3rd cycle) from 0.1 A g^{-1} to 1 A g^{-1}, the FS@TO delivers 465.3 mA h g^{-1} in the 4th cycle and retains 402.5 mA h g^{-1} in the 500th cycle; the capacity retention is as high as 86.5% and the capacity fading rate is only 0.03% per cycle. Contrastingly, the FS electrode delivers 506.9 mA h g^{-1} in the fourth cycle, even slightly higher than that of FS@TO, but only retains 58.8% of this capacity after being cycled for 230 times at 1 A g^{-1} (Fig. S10c†). These results strongly support that combining the high capacity conversion type anode material FeS with robust and flexible amorphous TiO_2/C nanofiber backbones is an efficient way to improve its cycling stability. And as mentioned above, the amorphous TiO_2 also played an important role in preventing the FeS crystals from growing too large by slowing down the outward motion of iron species during the sulfurization, thus successfully maintaining the nanofibrous morphology, which also ensured the superb cycling performance of FS@TO. The electrochemical performances of FS@TO samples sulfurized at different temperatures are compared in Fig. S13.† As it can be seen, although also supported by robust and stable amorphous TiO_2 backbones, FS@TO-600 and FS@TO-700 exhibit poorer rate performances than FS@TO. This should be ascribed to the smaller crystal size and richer defects in FS@TO, which ensure faster kinetics and higher pseudocapacitance.

For better understanding the electrochemical kinetics of FS@TO nanofibers, cyclic voltammetry (CV) tests were conducted at different scanning rates from 0.1 to 2 mV s^{-1}. As shown in Fig. 5a, CV curves obtained at different sweep rates are similar in shape with a slight peak shift as the scan rate increases, which indicates the excellent kinetics and low polarization of the FS@TO electrode at high sweep rates. According to Bruce Dunn *et al.*,[72] materials with high surface area and complex structures tend to have a high portion of external pseudocapacitance contribution. The relationship between the measured current (i) and the corresponding scan rates (v) can be described by the following equations:[73]

$$I(V) = av^b, \tag{1}$$

$$I(V) = k_1v + k_2v^{1/2} \tag{2}$$

where a and b are two adjustable parameters, v is the sweep rate (mV s^{-1}) and $I(V)$ is the current (mA) at the corresponding sweep rate.[73] The storage mechanism can be distinguished by the range of the b value, which can be obtained from the slope of the log(v) *vs.* log(I) plot (Fig. 5b). The value of b varies from 0.5 to 1 corresponding to different lithium ion storage mechanisms. If the b value is close to 0.5, then the system is controlled by diffusion, whereas if the b value is equal to 1, then it means it is a capacitive process. With regard to peak 1, 2 and 3, the b values are 0.866, 0.824 and 0.860, respectively, indicating that the kinetics of the FS@TO are mainly surface capacitive-controlled.[74] However, the fitted b values of peak 1 and 2 of the FS sample are 0.458 and 0.513 (Fig. S14a and b†), respectively, suggesting that the corresponding lithiation/delithiation processes are diffusion controlled.

According to eqn (2), where k_1 and k_2 are parameters for a given potential, k_1v represents the contribution of the capacitive process, whereas $k_2v^{1/2}$ indicates the contribution of the diffusion-controlled process. For analytical purpose, eqn (2) can be rearranged to:

$$I(V)/v^{1/2} = k_1v^{1/2} + k_2 \tag{3}$$

In this way, the values of k_1 (slope) and k_2 (intercept) can be obtained from the fitted straight line. Based on the quantification, the capacitive-controlled contribution was calculated to be 83.5% for FS@TO at a scan rate of 1 mV s^{-1} (Fig. 5c). Fig. 5d shows the percentage of the pseudocapacitive contribution at various scan rates, which gradually increases with higher sweep speed. For comparison, the capacitive contribution percentages in FS and TO electrodes at different scan rates were also calculated and are presented in Fig. S14d and S11d,† respectively, which are much smaller than those in FS@TO. This result explains why FS@TO delivers much better rate performances than FS and TO.

It is well known that the overall performance of a battery, especially its rate performance, greatly depends on the diffusion rate of lithium ions in the electrode material. In other words, it is very useful to determine the chemical diffusion coefficient for studying the electrochemical properties of materials. Therefore, electrochemical impedance spectroscopy (EIS) and the Galvanostatic Intermittent Titration Technique (GITT) (before the EIS and GITT tests, all batteries were cycled 50 times at a current density of 0.5 A g^{-1} to stabilize the batteries) were carried out. Fig. 6a displays the Nyquist plots. The semicircle represents the high frequency region, and the straight line corresponds to the low frequency region. According to eqn (S1)[34] (ESI†), the diffusion coefficient of lithium ions is inversely proportional to the value of the square of the slope σ. As shown in Fig. 6b, the slopes of the FS@TO, FS and TO electrodes are 280.4, 206.4 and 565.2, respectively. Therefore, according to the EIS results, FS has the highest diffusion coefficient, which is slightly larger than that of FS@TO and much larger than that of TO. Considering the intrinsic good electronic and ionic conductivity of iron sulfide, the result is reasonable as the FS sample has the largest portion of FeS. As for the FS@TO sample, although a little of its good conductivity and diffusive activity was sacrificed due to combining with TiO_2, it gained much better structural stability and a fine crystal size in return which ensured its superior overall cycling performance and rate capability.

Fig. 6c displays the charge/discharge profiles of the FS@TO electrode in the GITT test along with the corresponding diffusion coefficients of FS@TO, FS and TO, which were calculated based on eqn (S2) (ESI†). As it can be seen, the diffusion coefficients of FS@TO and FS electrodes are comparable and much higher (more than one magnitude) than those of the TO electrode. The diffusion coefficients of TO vary in a flat and consecutive trend, revealing its amorphous feature, while those of FS fluctuate much more drastically. As for the FS@TO sample, its diffusion coefficients also fluctuate during the lithiation and delithiation processes due to the phase transition of FeS, but in a more flat way than that of the FS sample, which should be attributed to its robust TiO_2 backbones and much smaller crystal size of FeS nanosheets. And it is worth mentioning that the diffusion coefficients of the FS sample are much lower than those of FS@TO at around 1.5 V in discharge and around 2.0 V in charge (marked by red dashed line circles), in contrast to the fact that they are slightly higher for most of the time during the test. This phenomenon strongly supports the conclusion that the FS sample suffers a much more violent volume expansion than FS@TO. This conclusion is confirmed by the post-cycling SEM images of FS@TO, FS and TO electrodes, as shown in Fig. S16.† After being cycled at 0.5 A g^{-1} for 50 cycles, FS@TO and TO electrodes can still maintain the spacious nanofibrous morphology, while the FS electrode shows a dense and compact morphology with obvious agglomerations. The TEM image of the FS@TO electrode after cycling at 0.5 A g^{-1} for 50 times shown in Fig. S17a† further revealed that the FeS nanosheets are still steadily attached to the surface of the TiO_2 nanofibers. However, the structure of FS collapses (Fig. S17b†) due to the violent volume fluctuations during repeated (de)lithiation.

To further demonstrate the potential practical application of the FS@TO sample, a lithium-ion full battery was assembled by pairing with a commercial $LiFePO_4$ cathode, as illustrated in Fig. 7a. A prelithiation procedure for FS@TO was carried out in a half-cell to compensate for the lithium loss during the initial cycle. In order to ensure the full utilization of the FS@TO electrode, the full-cell was assembled based on the capacity ratio of 1.2 : 1 between $LiFePO_4$ and FS@TO. And the capacity of the full-cell was calculated using the active mass of the FS@TO electrode only. The charge/discharge profiles of selected cycles for the lithium ion full-cell (voltage window is 1.0–3.7 V) at

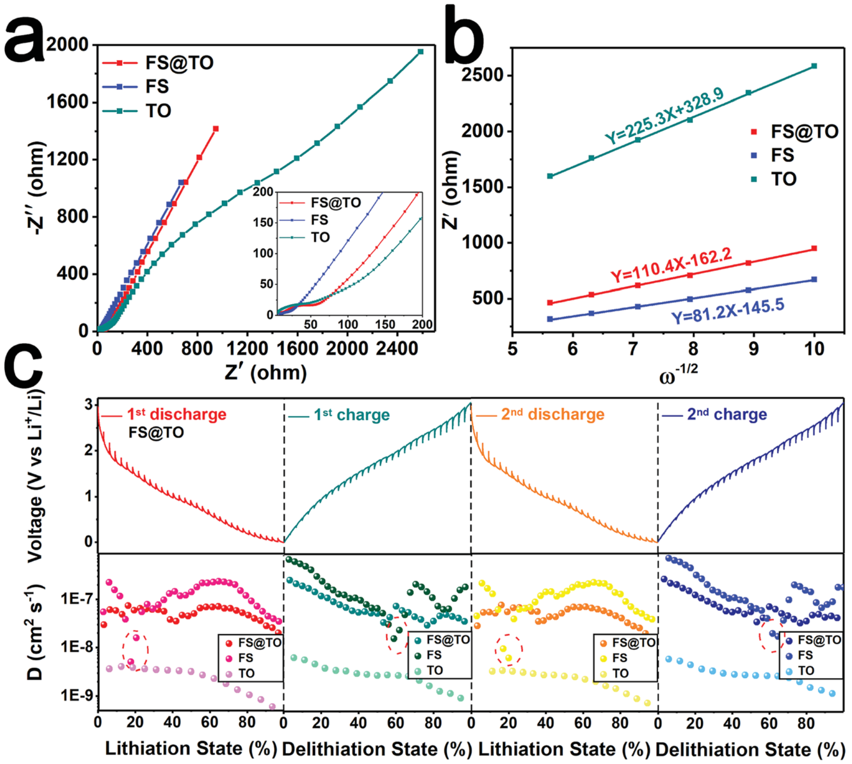

Fig. 6 EIS spectra (a) of FS@TO, FS, and TO electrodes, and the corresponding details in the high frequency region (inset of (a)); the *linear* relationship plot (b) of Z' *versus* $\omega^{-1/2}$ at the low-frequency region; GITT curves and the corresponding Li^+ diffusion coefficient (c) at different discharge/charge states of the FS@TO electrode.

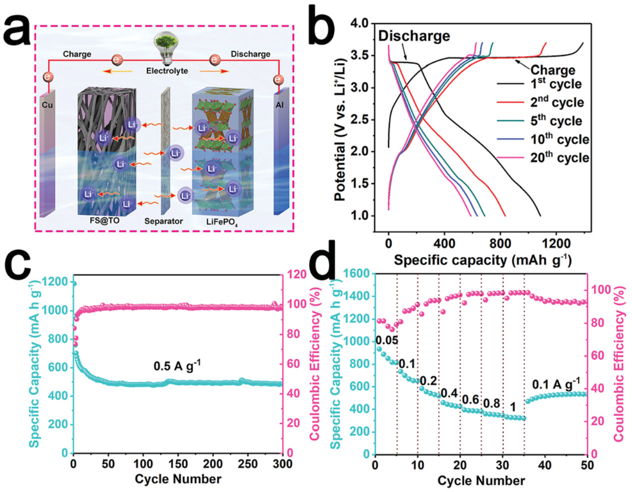

Fig. 7 Lithium-ion full-cell electrochemical performance. (a) Schematic illustration of the $LiFePO_4$//FS@TO full-cell, (b) the charge/discharge profiles of the selected cycles in the potential range of 1.0–3.7 V at a current density of 0.1 A g^{-1}, (c) the cycling performance at a current density of 0.5 A g^{-1}, and (d) the rate performance from 0.05 to 1 A g^{-1}.

a current density of 0.1 A g^{-1} is shown in Fig. 7b. From the 5th to 20th cycles, the charge/discharge curves are almost coincident, showing highly reversible charge/discharge behavior. When being cycled at 0.5 A g^{-1} (the first two cycles were tested at 0.1 A g^{-1} for better activation), the full-cell also displays excellent cycling stability with a high coulombic efficiency of around 97% throughout the 300-cycle test (Fig. 7c), except for the first few cycles, in which the coulombic efficiency is relatively low due to the formation of a SEI layer. The rate performance of the full-cell has also been investigated and results are shown in Fig. 7d. High discharge capacities of 932.9 to 812.8, 734.4 to 651.1, 583.7 to 517.7, 434.7, 386.1, 351.6, 324.4, and 514.4 mA h g^{-1} were delivered at the current densities of 0.05, 0.1, 0.2, 0.4, 0.6, 0.8, 1.0 and 0.1 A g^{-1}, respectively (Fig. 7d). The good rate performance can be ascribed to the small crystal size of FeS nanosheets, durable amorphous TiO_2 backbones, highly conductive carbonaceous matrix and good lithium ion diffusive ability of FeS in the composite anode materials.

Conclusions

In summary, a composite anode material with a novel hierarchical structure of nitrogen-doped carbon nanofiber wrapped FeS nanosheets grown on amorphous TiO_2 backbones has been successfully *in situ* synthesized *via* the electrospinning technique and subsequent *in situ* conversion with vacuum sulfurization. The influence of temperature on the morphology of sulfurized products was also investigated, and 500 °C was found to be the best, which not only successfully maintained the nanofibrous structure but also prevented the FeS crystals from growing too large, thus ensuring superior cycling stability and rate performance. The addition of a titanium source was also found to be critical in suppressing the uncontrolled growth of FeS and offered a durable backbone support as well. With such a structural advantage and synergistic effect, the as-synthesized FS@TO sample exhibited the best rate performance and cycling stability when compared with single-component FeS and TiO_2. A high reversible specific capacity of 465 mA h g^{-1} can be delivered by FS@TO at 2 A g^{-1} and when being cycled at 1 A g^{-1}, and its capacity fading rate is as low as 0.03% per cycle. Moreover, the $LiFePO_4$//FS@TO full-cell also shows good rate performance and stable long-term cycling ability, and a high coulombic efficiency of around 97% was obtained at a current density of 0.5 A g^{-1} throughout a 300-cycle test with a reversible specific capacity of 485.7 mA h g^{-1}. As the industrial requirements of lithium ion batteries are surging, this work would be enlightening for pursuing durable and high performance anode materials for practical applications.

Conflicts of interest

There are no conflicts to declare.

Acknowledgements

This work was supported by the Natural Science Foundation of Hunan Province in China (2018JJ1036), the National Natural Science Foundation of China (No. 51874362), and Hunan Provincial Innovation Foundation for Postgraduate (Grant No. CX2015B040).

References

1 Z. Hu, Z. Zhu, F. Cheng, K. Zhang, J. Wang, C. Chen and J. Chen, *Energy Environ. Sci.*, 2015, **8**, 1309–1316.

2 Z. Liu, T. Lu, T. Song, X.-Y. Yu, X. W. D. Lou and U. Paik, *Energy Environ. Sci.*, 2017, **10**, 1576–1580.

3 H. Fan, H. Yu, X. Wu, Y. Zhang, Z. Luo, H. Wang, Y. Guo, S. Madhavi and Q. Yan, *ACS Appl. Mater. Interfaces*, 2016, **8**, 25261–25267.

4 Y. Xiao, S. H. Lee and Y. K. Sun, *Adv. Energy Mater.*, 2017, **7**, 1601329.

5 M.-R. Gao, Y.-F. Xu, J. Jiang and S.-H. Yu, *Chem. Soc. Rev.*, 2013, **42**, 2986–3017.

6 C. Zhu, X. Mu, P. A. van Aken, Y. Yu and J. Maier, *Angew. Chem., Int. Ed.*, 2014, **126**, 2184–2188.

7 L. Yu, J. F. Yang and X. W. Lou, *Angew. Chem., Int. Ed.*, 2016, **55**, 13422–13426.

8 X. Nie, X. Kong, D. Selvakumaran, L. Lou, J. Shi, T. Zhu, S. Liang, G. Cao and A. Pan, *ACS Appl. Mater. Interfaces*, 2018, **10**, 36018–36027.

9 J. Huang, Z. Wei, J. Liao, W. Ni, C. Wang and J. Ma, *J. Energy Chem.*, 2019, **33**, 100–124.

10 Z. Wei, L. Wang, M. Zhuo, W. Ni, H. Wang and J. Ma, *J. Mater. Chem. A*, 2018, **6**, 12185–12214.

11 X. Wei, W. Li, J.-a. Shi, L. Gu and Y. Yu, *ACS Appl. Mater. Interfaces*, 2015, **7**, 27804–27809.

12 Q. T. Xu, H. G. Xue and S. P. Guo, *Inorg. Chem. Front.*, 2018, **5**, 2540–2545.

13 Q. Ma, H. Song, Q. Zhuang, J. Liu, Z. Zhang, C. Mao, H. Peng, G. Li and K. Chen, *Chem. Eng. J.*, 2018, **338**, 726–733.

14 X. Wei, X. Tan, J. Meng, X. Wang, P. Hu, W. Yang, S. Tan, Q. An and L. Mai, *Nano Res.*, 2018, **11**, 6206–6216.

15 M. Huang, A. Xu, H. Duan and S. Wu, *J. Mater. Chem. A*, 2018, **6**, 7155–7161.

16 B. Wu, H. Song, J. Zhou and X. Chen, *Chem. Commun.*, 2011, **47**, 8653–8655.

17 G. Fang, Z. Wu, J. Zhou, C. Zhu, X. Cao, T. Lin, Y. Chen, C. Wang, A. Pan and S. Liang, *Adv. Energy Mater.*, 2018, **8**, 1703155.

18 D. Li, D. Yang, X. Yang, Y. Wang, Z. Guo, Y. Xia, S. Sun and S. Guo, *Angew. Chem., Int. Ed.*, 2016, **55**, 15925–15928.

19 P. Ramakrishnan, S.-H. Baek, Y. Park and J. H. Kim, *Carbon*, 2017, **115**, 249–260.

20 J. Wang, H. He, Z. Wu, J. Liang, L. Han, H. L. Xin, X. Guo, Y. Zhu and D. Wang, *J. Power Sources*, 2018, **392**, 193–199.

21 J. S. Cho, J.-S. Park and Y. C. Kang, *Nano Res.*, 2016, **10**, 897–907.

22 S. Liu, Z. Cai, J. Zhou, M. Zhu, A. Pan and S. Liang, *J. Mater. Chem. A*, 2017, **5**, 9169–9176.

23 L. Wu, J. Zheng, L. Wang, X. Xiong, Y. Shao, G. Wang, J. H. Wang, S. Zhong and M. Wu, *Angew. Chem., Int. Ed.*, 2019, **58**, 811–815.

24 W. Ni, B. Wang, J. Cheng, X. Li, Q. Guan, G. Gu and L. Huang, *Nanoscale*, 2014, **6**, 2618–2623.

25 Q. Ma, Q. Zhuang, J. Liang, Z. Zhang, J. Liu, H. Peng, C. Mao and G. Li, *Nanomaterials*, 2017, **7**, 431.

26 W. Li, L. Zeng, Y. Wu and Y. Yu, *Sci. China Mater.*, 2016, **59**, 287–321.

27 Z. Liang, G. Zheng, W. Li, Z. W. Seh, H. Yao, K. Yan, D. Kong and Y. Cui, *ACS Nano*, 2014, **8**, 5249–5256.

28 J. Yang, Y. Wang, W. Li, L. Wang, Y. Fan, W. Jiang, W. Luo, Y. Wang, B. Kong, C. Selomulya, H. K. Liu, S. X. Dou and D. Zhao, *Adv. Mater.*, 2017, **29**, 1700523.

29 J. Y. Cheong, C. Kim, J. W. Jung, T. G. Yun, D. Y. Youn, S. H. Cho, K. R. Yoon, H. Y. Jang, S. W. Song and I. D. Kim, *J. Power Sources*, 2018, **400**, 485–492.

30 Z. Li, J. Zhang, B. Guan, D. Wang, L. M. Liu and X. W. Lou, *Nat. Commun.*, 2016, **7**, 13065.

31 N. Wang, J. Yue, L. Chen, Y. Qian and J. Yang, *ACS Appl. Mater. Interfaces*, 2015, **7**, 10348–10355.

32 S. N. Liu, Z. G. Luo, G. Y. Tian, M. N. Zhu, Z. Y. Cai, A. Q. Pan and S. Q. Liang, *J. Power Sources*, 2017, **363**, 284–290.

33 J. Liang, Y. Jiao, M. Jaroniec and S. Z. Qiao, *Angew. Chem., Int. Ed.*, 2012, **124**, 11664–11668.

34 J. S. Cho, Y. J. Hong and Y. C. Kang, *ACS Nano*, 2015, **9**, 4026–4035.

35 T. Ohsaka, F. Izumi and Y. Fujiki, *J. Raman Spectrosc.*, 1978, **7**, 321–324.

36 W. F. Zhang, Y. L. He, M. S. Zhang, Z. Yin and Q. Chen, *J. Phys. D: Appl. Phys.*, 2000, **33**, 912–916.

37 A. Boughriet, R. S. Figueiredo, J. Laureyns and P. Recourt, *J. Chem. Soc., Faraday Trans.*, 1997, **93**, 3209–3215.

38 E. B. Hansson, M. S. Odziemkowski and R. W. Gillham, *Corros. Sci.*, 2006, **48**, 3767–3783.
39 Y. Xu, W. Li, F. Zhang, X. Zhang, W. Zhang, C.-S. Lee and Y. Tang, *J. Mater. Chem. A*, 2016, **4**, 3697–3703.
40 L. Shi, D. Li, J. Yu, H. Liu, Y. Zhao, H. Xin, Y. Lin, C. Lin, C. Li and C. Zhu, *J. Mater. Chem. A*, 2018, **6**, 7967–7976.
41 K. Shimada, T. Mizokawa, K. Mamiya, T. Saitoh, A. Fujimori and T. Kamimura, *Surf. Sci. Spectra*, 1999, **6**, 321–336.
42 C. Xu, Y. Zeng, X. Rui, N. Xiao, J. Zhu, W. Zhang, J. Chen, W. Liu, H. Tan, H. H. Hng and Q. Yan, *ACS Nano*, 2012, **6**, 4713–4721.
43 J. Luo, J. Liu, Z. Zeng, C. F. Ng, L. Ma, H. Zhang, J. Lin, Z. Shen and H. J. Fan, *Nano Lett.*, 2013, **13**, 6136–6143.
44 Z. Yi, Q. Han, S. Ju, Y. Wu, Y. Cheng and L. Wang, *J. Electrochem. Soc.*, 2016, **163**, A2641–A2646.
45 M. Madian, M. Klose, T. Jaumann, A. Gebert, S. Oswald, N. Ismail, A. Eychmüller, J. Eckert and L. Giebeler, *J. Mater. Chem. A*, 2016, **4**, 5542–5552.
46 Q. Tian, Z. Zhang, L. Yang and S.-i. Hirano, *J. Power Sources*, 2014, **253**, 9–16.
47 Y. Wang, Y. Zhang, J. Shi, X. Kong, X. Cao, S. Liang, G. Cao and A. Pan, *Energy Storage Materials*, 2019, **18**, 366–374.
48 S. Peng, X. Han, L. Li, Z. Zhu, F. Cheng, M. Srinivansan, S. Adams and S. Ramakrishna, *Small*, 2016, **12**, 1359–1368.
49 B. Yin, X. Cao, A. Pan, Z. Luo, S. Dinesh, J. Lin, Y. Tang, S. Liang and G. Cao, *Adv. Sci.*, 2018, **5**, 1800829.
50 L.-L. Feng, G.-D. Li, Y. Liu, Y. Wu, H. Chen, Y. Wang, Y.-C. Zou, D. Wang and X. Zou, *ACS Appl. Mater. Interfaces*, 2015, **7**, 980–988.
51 Y. Wang, Y. Zhang, J. Shi, A. Pan, F. Jiang, S. Liang and G. Cao, *J. Mater. Chem. A*, 2018, **6**, 18286–18292.
52 Q. Guo, Y. Ma, T. Chen, Q. Xia, M. Yang, H. Xia and Y. Yu, *ACS Nano*, 2017, **11**, 12658–12667.
53 W. Chen, J. Pei, C. T. He, J. Wan, H. Ren, Y. Zhu, Y. Wang, J. Dong, S. Tian and W. C. Cheong, *Angew. Chem., Int. Ed.*, 2017, **129**, 16302–16306.
54 L. Zhou, K. Zhang, J. Sheng, Q. An, Z. Tao, Y.-M. Kang, J. Chen and L. Mai, *Nano Energy*, 2017, **35**, 281–289.
55 Y. Zhang, A. Pan, L. Ding, Z. Zhou, Y. Wang, S. Niu, S. Liang and G. Cao, *ACS Appl. Mater. Interfaces*, 2017, **9**, 3624–3633.
56 P. Ganesan, M. Prabu, J. Sanetuntikul and S. Shanmugam, *ACS Catal.*, 2015, **5**, 3625–3637.
57 J. Chen, A. Pan, Y. Wang, X. Cao, W. Zhang, X. Kong, Q. Su, J. Lin, G. Cao and S. Liang, *Energy Storage Materials*, 2019, DOI: 10.1016/j.ensm.2018.10.019.
58 D. H. Liu, W. H. Li, Y. P. Zheng, Z. Cui, X. Yan, D. S. Liu, J. Wang, Y. Zhang, H. Y. Lü and F. Y. Bai, *Adv. Mater.*, 2018, **30**, 1706317.
59 J. R. Shi, Y. P. Wang, Q. Su, F. Y. Cheng, X. Z. Kong, J. D. Lin, T. Zhu, S. Q. Liang and A. Q. Pan, *Chem. Eng. J.*, 2018, **353**, 606–614.
60 Y. Kim and J. B. Goodenough, *J. Phys. Chem. C*, 2008, **112**, 15060–15064.
61 D. W. Wang, G. Zhou, F. Li, K. H. Wu, G. Q. Lu, H. M. Cheng and I. R. Gentle, *Phys. Chem. Chem. Phys.*, 2012, **14**, 8703–8710.
62 T. Yim, M.-S. Park, J.-S. Yu, K. J. Kim, K. Y. Im, J.-H. Kim, G. Jeong, Y. N. Jo, S.-G. Woo, K. S. Kang, I. Lee and Y.-J. Kim, *Electrochim. Acta*, 2013, **107**, 454–460.
63 J. Gao, M. A. Lowe, Y. Kiya and H. D. Abruña, *J. Phys. Chem. C*, 2011, **115**, 25132–25137.
64 S. S. Zhang, *Front. Energy Res.*, 2013, **1**, 10.
65 X. Wang, Q. Xiang, B. Liu, L. Wang, T. Luo, D. Chen and G. Shen, *Sci. Rep.*, 2013, **3**, 2007.
66 L. Li, C. Gao, A. Kovalchuk, Z. Peng, G. Ruan, Y. Yang, H. Fei, Q. Zhong, Y. Li and J. M. Tour, *Nano Res.*, 2016, **9**, 2904–2911.
67 L. Fei, Q. Lin, B. Yuan, G. Chen, P. Xie, Y. Li, Y. Xu, S. Deng, S. Smirnov and H. Luo, *ACS Appl. Mater. Interfaces*, 2013, **5**, 5330–5335.
68 C. Xing, D. Zhang, K. Cao, S. Zhao, X. Wang, H. Qin, J. Liu, Y. Jiang and L. Meng, *J. Mater. Chem. A*, 2015, **3**, 8742–8749.
69 C. Zhu, Y. Wen, P. A. van Aken, J. Maier and Y. Yu, *Adv. Funct. Mater.*, 2015, **25**, 2335–2342.
70 J. Zhao, J. A. Syed, X. Wen, H. Lu and X. Meng, *J. Alloys Compd.*, 2019, **777**, 974–981.
71 C. Dong, X. Zheng, B. Huang and M. Lu, *Appl. Surf. Sci.*, 2013, **265**, 114–119.
72 V. Augustyn, P. Simon and B. Dunn, *Energy Environ. Sci.*, 2014, **7**, 1597–1614.
73 V. Augustyn, J. Come, M. A. Lowe, J. W. Kim, P.-L. Taberna, S. H. Tolbert, H. D. Abruña, P. Simon and B. Dunn, *Nat. Mater.*, 2013, **12**, 518.
74 D. Chao, P. Liang, Z. Chen, L. Bai, H. Shen, X. Liu, X. Xia, Y. Zhao, S. V. Savilov and J. Lin, *ACS Nano*, 2016, **10**, 10211–10219.